



# Perineural Invasion Detection Using Deep Learning: A Systematic Review

Hayagreev Jeyandran <sup>1\*</sup> and Dr. Veena R, MD <sup>2</sup>

<sup>1</sup>Intern - Deep Learning Researcher, Department of Histopathology, HealthCare Global Enterprises Ltd., Bengaluru, India.

<sup>2</sup>Senior Consultant Pathologist and Head of the Department of Histopathology and Digital Pathology, Triesta Sciences - A unit of HealthCare Global Enterprises Ltd., Bengaluru, India.

\*Corresponding author(s). E-mail(s): [hayagreevj@gmail.com](mailto:hayagreevj@gmail.com);  
Contributing authors: [drveena.r@hcgel.com](mailto:drveena.r@hcgel.com);

## Acknowledgments

This work was conducted at the Department of Histopathology and Digital Pathology, HealthCare Global (HCG) hospital KR Road, Bengaluru. It was presented at the proceedings of the HCG Tumor Board in October 2024.

## Abstract

Perineural Invasion (PNI) is the infiltration of tumour cells into the perineurium, a protective sheath surrounding nerve tissue. It is a critical pathological marker associated with poor prognosis in various types of cancers, such as pancreatic, rectal, head and neck, and prostate. It has been associated with cancer recurrence and metastasis, however, detecting PNI in whole-slide pathological images remains a laborious and error-prone task for pathologists, resulting in significant implications for treatment planning. This paper surveys cutting-edge deep learning approaches applied to PNI diagnosis, offering a structured segmentation, detection and classification model taxonomy. In doing so, gaps in existing literature, such as model robustness and clinical integration, are identified, culminating in future research directions to integrate these models into clinical practice for more accurate and scalable PNI diagnosis.

**Keywords:** Perineural Invasion, Histopathology, Whole Slide Images, Deep Neural Networks

# 1 Introduction

Perineural Invasion (PNI) was first identified as the invasion of neoplastic cancer cells into, around, and through nerves [1]. However, it has a more precise definition concerning the peripheral nerve sheath.

## 1.1 Structure of the Peripheral Nerve Sheath

The layers are listed from outer-most to inner-most [2].

- Epineurium: Dense elastin and collagen connective tissue. It surrounds the entire nerve and contains its vascular supply.
- Perineurium: Endothelial cells with basal laminae that tightly fit axons and form a selectively permeable membrane.
- Endoneurium: An uninterrupted sheath that contains single nerve fibres myelinated by Schwann cells. It is made of delicate connective tissue running uninterrupted from the brain to the spinal cord. This layer also contains endoneurial fluid, a major component of the blood-nerve barrier.

PNI is the presence of a tumour in any of these layers. Many pathologists classify the encircling of 33% of a nerve by tumour cells as PNI. Nevertheless, presence within the layers might be more clinically relevant [3]. There have been a multitude of earlier theories governing PNI, namely that it is an extension of lymphatic metastasis [4] and that the nerve sheath provides a conduit of low resistance for tumour spread [5]. However, both these theories were disproven subsequently. The current hypothesis is that the host and cancer share a mutual relationship in fuelling the extent of PNI [6]; the nerve micro-environment (macrophages, fibroblasts, Schwann cells), molecular signalling (such as neurotrophic factors, extracellular matrices, chemokines, axonal guidance) might have a role to play. This is still under investigation even today [6], leaving us with a lack of targeted therapies for PNI.

## 1.2 Occurrence and Prognostic significance

Notwithstanding the molecular mechanisms of PNI remaining largely unknown, plenty of evidence from various types of cancers collected over a long period suggests that PNI is of prognostic significance, contributing to recurrence. For example, Zhang et al. evaluated the association between PNI and biochemical recurrence in cases of prostate cancer [7]. The prognostic role of PNI in surgically treated oesophageal squamous cell carcinoma [8], gastric cancer [9] [10] and its impact on the 5-year survival of stage 1 - 3 rectal cancer patients [11] have been examined previously. Even for trained pathologists, detecting PNI from Whole-Slide Images (WSIs) is laborious for the following reasons.

1. **Microscopic Structures** - Nerves on WSIs, especially small peripheral ones, are difficult to distinguish from benign glands, blood vessels, and muscle fibres.
2. **Morphology** - Tumor can invade nerves in various ways. The visual appearance of PNI varies depending on histology and organ type.

3. **Sparsity** - PNI can occur in isolated regions that are sparse and scattered throughout large WSIs, making them difficult to detect.

These challenges result in inter-observer and intra-observer variability while manually examining slides for PNI [12]. In a study on squamous cell carcinoma of the vulva, the authors stipulate that 27% of examined cases were reported as PNI absent while PNI was present [13]. Similarly, in a study involving colorectal cancer, the percentage of patients initially diagnosed as PNI positive increased from 7.5% to 24.3% following a meticulous second review by pathologists [14]. The intestinal wall is a dense structure whose complexity can easily overshadow subtle infiltration into the nerves. Interestingly, variability in the diagnosis of oral squamous cell carcinoma was attributed to a lack of clarity on what constituted PNI in a study by Yan et al [15]. All of these lapses point us toward the need for assistive technology to at least aid pathologists by automatically flagging a WSI in case of suspected PNI. A pathologist can review the case and model’s predictions more carefully subsequently.

### 1.3 Deep Learning in Medical Imaging

Deep Learning (DL), a subset of Artificial Intelligence, has revolutionized the field of medical imaging by enabling computers to automatically analyze complex patterns in medical data (CT, MRI, X-rays, and Pathology Images) with remarkable accuracy. DL systems are capable of automatically extracting relevant features without the need for manual feature engineering [16]. Several studies over the years have tuned DL implementations to support diagnostic functionality. For example, a Convolutional Neural Network was used by Nirschl J. et al. to detect signs of clinical heart failure from Hematoxylin and Eosin (H&E) stained WSIs [17]. Other advances include two-stage glomerular segmentation [18] and multi-instance gastric image segmentation [19]. DL has also been applied to PNI diagnosis before, although in a very limited number of studies. The following sections will thoroughly examine these studies. In section 2, the literature is introduced and grouped into various categories. Following this, the dataset and pre-processing methods are elucidated. Then, the neural network models, training strategies, and post-processing techniques are explained. Following this, evaluation metrics for the models and error analysis of the algorithm’s performance are examined. Lastly, future research scope is suggested before concluding.

## 2 Summary of Approaches

Most computer vision problems can be largely classified as either **classification**, **object detection**, or **image segmentation** [20]. In classification, the model only outputs probabilities for the entire image/input. In object detection, the model outputs bounding box coordinates of features within the image, such as tumours and nerves. Lastly, segmentation is when the model outputs pixel-wise probabilities for the entire image, producing a segmentation *mask*. This is a binary mask made from thresholding the pixel-wise probabilities (eg: regions containing PNI) and can be likened to shading relevant regions in the image. This system of classification is also maintained in the context of PNI detection. Most approaches directly utilize an end-to-end model

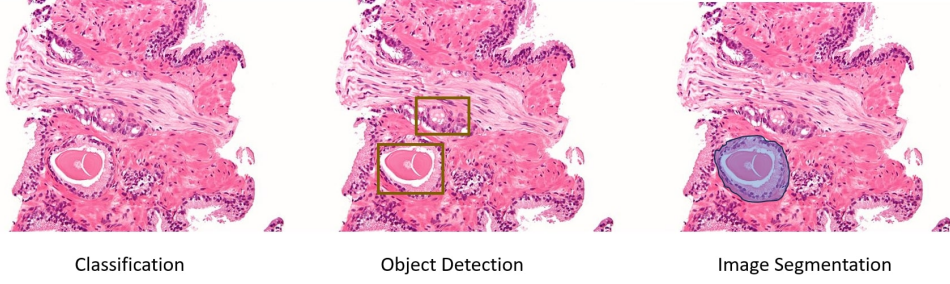


**Fig. 1:** Example of DL approaches applied to gland detection on a WSI. Image source: [Wikimedia](#), licensed under CC BY-SA 3.0. Modifications made by the author.

and segment either the boundary between the tumour and nerve (known as the PNI Junction) or the PNI field (region) from the WSIs. The other approach is to use a sequential pipeline, where segmentation or object detection is used for tumour and nerve fields in the first two stages respectively. Then, a rule-based classifier identifies PNI based on the proximity or overlap of the outputs of the two stages. The first approach is less complex and requires fewer annotations, whereas the second approach is more sophisticated and allows for greater analysis due to the orthogonalization used.

**Table 1:** Reviewed Literature

Literature	Approach	Authors
Automated Hybrid Model for Detecting Perineural Invasion in the Histology of Colorectal Cancer [21]	Multi-Class Tumor and Nerve Field Segmentation + Rule-Based PNI Classifier	Jiyeon Jung et al.
Perineural Invasion Detection in Multiple Organ Cancer Based on Deep Convolutional Neural Network [22]	PNI Junction Segmentation	Ramin Nateghi et al.
Efficient Perineural Invasion Detection of Histopathological Images Using U-Net (Multi-Organ Cancer) [23]	PNI Junction Segmentation	Youngjae Park et al.
Perineural invasion detection in pancreatic ductal adenocarcinoma using artificial intelligence [24]	Hierarchical Contextual Analysis, Binary Tumor and Nerve Field Segmentation + Rule-Based PNI Classifier	Kimmo Kartasalo et al.
Detection of perineural invasion in prostate needle biopsies with deep neural networks [25]	Binary PNI Field Segmentation	Ziwei Hu et al.
A multi-task deep learning framework for perineural invasion recognition in gastric cancer whole slide images [26]	Binary Tumor Field Segmentation and Nerve Object Detection + Rule-Based PNI Classifier	Ming Du et al.

### 3 Dataset

In the modern DL era, visual training tasks such as traditional image classifiers and macroscopic object detectors use large corpora of 1 - 10 million training images to

mitigate over-fitting and learn nuanced features [27]. Working with a similarly large number of whole WSIs for PNI detection is infeasible due to the following reasons:

1. **Computational Resources** - WSIs are high-resolution images, often with gigapixel sizes. Processing them like traditional images would require extensive storage and powerful GPUs or TPUs, which are usually not accessible in a medical research environment.
2. **Annotation and Labelling** - Annotating WSIs requires the expertise of trained pathologists, who are limited in number. Precise annotations are time-consuming and expensive for a large dataset ( $> 1000$  images) even with a large group of dedicated pathologists.
3. **Dimensionality** - WSIs show high morphological diversity. Each feature can be regarded as a separate pixel.

Thus, most works utilize a limited pool of WSIs and have a more unconventional train/validation/test split, with a larger proportion being used for the latter two (eg: 60/20/20) to achieve statistical significance and robust accuracy metrics. Moreover, these reasons also underscore the importance of pre-processing to make the data learnable [28].

### 3.1 PAIP 2021 - Grand challenge

The Pathology in Artificial Intelligence (AI) Platform (PAIP) hosted a challenge in 2021: Perineural Invasion in Multiple Organ Cancer [29]. Authors of [22], [23] have taken part in this competition and utilized the dataset provided. The dataset consisted of **150 Training WSIs** (50 each of Colon, Prostate, and Pancreatic-Biliary duct cancer), **30 Validation WSIs**, **60 Testing WSIs** each scanned at **20X Magnification** by an **Aperio AT2 scanner** (Leica Biosystems, Nussloch, Germany). The raw resolution of each WSI was **60000 x 60000**. One-pixel thick binary masks annotating the PNI junction were also provided for all 240 WSIs.

### 3.2 STHLM3 - Prostate Biopsy cores

Between 2012 and 2014, a study was conducted in Stockholm County, Sweden, in which 59159 men were tested for high prostate-specific antigen (PSA) levels [30]. 7406 of these men were referred to a **10 - 12 core trans-rectal ultrasound guided biopsy**, resulting in **83,470 prostate cores**. The authors of [25] oversampled high-grade cancers suitable for training a neural network to identify features of nervous and neoplastic tissue and randomized 80% of all resulting cores into a train set and the remaining 20% into a test set. In all, the **train set** included **1141 subjects and 7045 cores, including 379 PNI positive cores** and the **test set** included **286 subjects and 1758 cores, including 196 PNI positive cores**.

### 3.3 Hospital-specific datasets

- In [21], **77 WSIs** from **63 subjects** with **colorectal cancer** were collected from St. Mary's Hospital (Catholic Kwandong University, Incheon, Korea). Pathologists manually selected **530 regions of interest (ROI)** from the 77 WSIs. 4 classes were

used - PNI, Non-PNI with nerve, Non-PNI with Tumor, and Normal, before slides were pre-processed into patches. Each patch was assigned to one of four classes.

- In [26], 143 train, 12 validation, and 60 test WSIs from **gastric cancer** patients were gathered at **20x magnification** in Fujian Cancer Hospital, China.
- In [24], **260 training** (206 randomly selected, 54 manually assigned by pathologists due to abundant tumour and nerve features), **168 validation and testing** WSIs from patients with pancreatic ductal adenoma were gathered at **40x magnification** in Sourasky Medical Center, Tel-Aviv.

The diversity and quality of datasets is of paramount importance to the algorithm’s performance. While these datasets provide a good starting point, in the long run, PNI detection will benefit from emphasis on data curation techniques that produce diverse datasets encompassing a wide range of cancer types with histological variations [31] to produce an algorithm adaptable to histological tissue from any resected part of the body.

## 4 Pre-processing

### 4.1 Patching

To solve the problem of high dimensionality, most DL approaches include patching (tiling) as a mandatory pre-processing step [32]. Models are trained to make low-level predictions on each patch, and either max or average pooling is used over the entire slide to make higher-level predictions.

#### 4.1.1 Non-overlapping patches

In this approach, patches are given a fixed resolution of  $p \times p$ . A  $p \times p$  window is slid over the entire  $n_H \times n_W$  image with a stride of  $p$  in both the horizontal and vertical directions. If  $n_H \nmid p$  or  $n_W \nmid p$ , there will be left-over regions that do not fully fit the window. This can be dealt with in two ways: either by applying padding of  $p - (n_H \bmod p) \times p - (n_W \bmod p)$  or by considering the smaller, remaining regions at the edge of the image as another patch, resulting in  $\left\lceil \frac{n_H}{p} \right\rceil \times \left\lceil \frac{n_W}{p} \right\rceil$  patches. The first approach is preferred as it maintains consistency of input dimension into the model. Non-overlapping patches are used in [25] where  $p$  is specified as  $0.25mm$  and [22] where  $p = 512px$ . This may result in a loss of information from the boundary regions, which is dealt with using dilation techniques later on in the pre-processing pipeline.

#### 4.1.2 Overlapping Patches

In this second approach, the stride is set to  $p(1 - \text{overlap proportion})$ . Information is preserved in the boundary regions leading to more robust feature extraction at the cost of duplication. [26], [23], [21] all use this strategy with  $p$  ranging from 512 to 2048 and a overlap proportion of 0.50. In [26], the patches are cropped at equal intervals to minimize duplication.

## 4.2 Boundary Dilation

In approaches [22], [23] (which use PNI junction segmentation), morphological dilation is applied to enlarge the 1-pixel thick PNI-nerve boundary lines. By enhancing clarity in the region, the model can learn more complex transitional features between normal nerve tissue and PNI. Morphological dilation involves a structuring element of a particular radius (eg: [22] uses a disk of radius 3px). The operator is slid over the boundary, and the maximum value of the pixels within the operator is cast onto the remaining pixels within the operator.

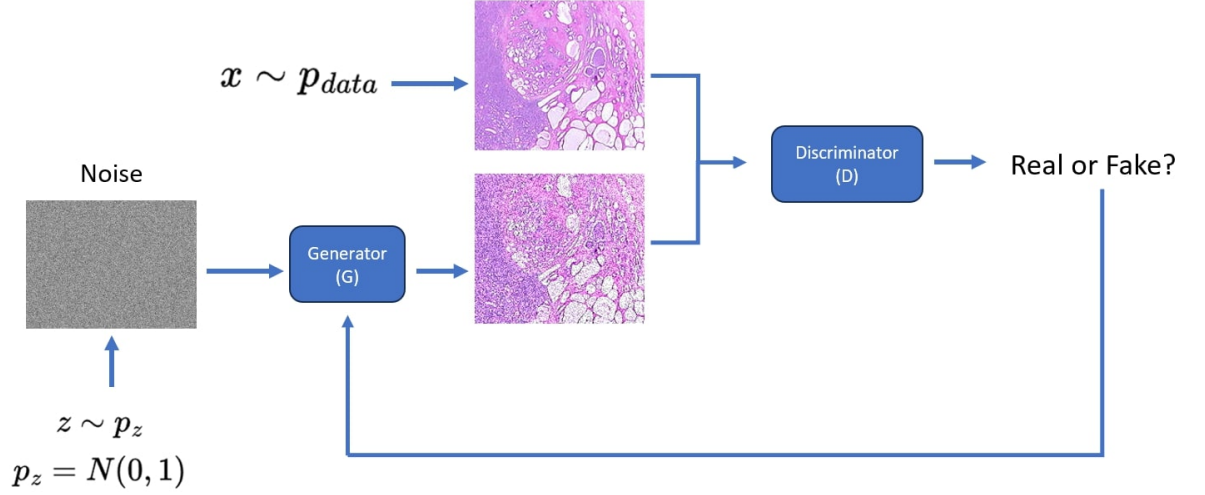


**Fig. 2:** GANs for WSIs: Framework. Source: [Wikimedia Commons](#) (licensed under CC-BY-SA 3.0). Modifications made by the author.

## 4.3 Data Augmentation

Data augmentation is a commonly used pre-processing technique and decreases vulnerability to over-fitting. It is important in medical imaging applications because of the limited availability of training data and lesser margin for error during real-world implementation [33]. All works for PNI detection use some form of data augmentation, such as colour augmentation (HSV), brightness and contrast adjustment, and geometric augmentation (rotation, flip, shear) at the individual patch level. In [24], synthetic data generation is utilized using **generative adversarial networks (GANs)** [34]. GANs consist of a generator  $G$  that produces synthetic images and a discriminator  $D$  that distinguishes between real and synthetic images, optimizing through a minimax game so  $G$  generates data similar to the real distribution. This synthetic generation and augmentation method can be seamlessly integrated into neural network pipelines using frameworks like TensorFlow [35] and PyTorch [36], enhancing model robustness against over-fitting.

## 4.4 Background Image Elimination

Works [21] and [26] examine pixel intensities to infer the usability of patches. For example, [26] considers  $\sigma_{pixelIntensity} < 0.6$  to be an indicator of a background image with no useful pathological features. [21] mandates that  $39 < \mu_{pixelIntensity} < 235$  for all patches. Anything higher is considered background, while any patches below the range are regarded as low quality and discarded.  $\sigma$  and  $\mu$  are the standard deviation and mean respectively.

## 5 Models and Training

### 5.1 Segmentation Models

#### 5.1.1 U-Net

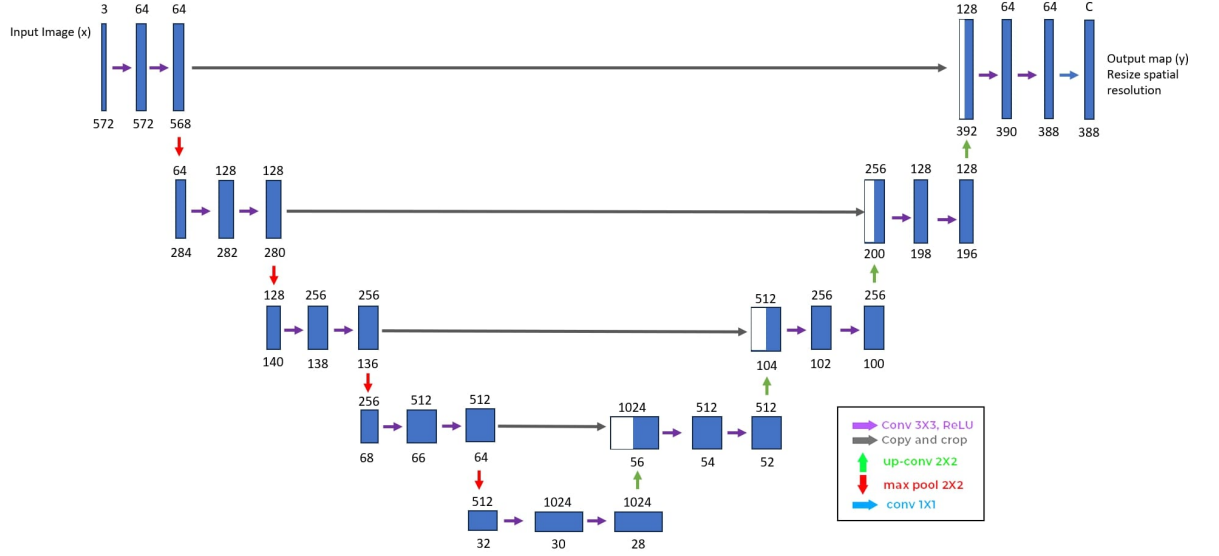


**Fig. 3:** UNet Architecture

Proposed in [37] by Ronneberger et al., U-Net has been a seminal integration into the field of medical imaging. All works except [22] make use of the basic U-Net architecture, some of them modifying part of it. Its distinctive feature is the symmetric structure, consisting of an **encoder** and a **decoder** connected by skip connections. Here are the functions of each part of the architecture:

- **Encoder:** Takes as input a WSI patch of resolution  $n_H, n_W, n_C$ . The encoder follows a contracting path, wherein repeated  $3 \times 3$  3D valid Convolutions are used to down sample  $n_H, n_W$  while increasing  $n_C$ . Max pooling operations with a window



size of  $2 \times 2$  are also applied after every two convolution operations. The encoder allows the network to capture higher-level features at multiple scales.

- **Bottleneck:** Deepest layer in the network. Images with the smallest spatial resolution and most abstract feature representations are processed using  $3 \times 3$  convolutions.
- **Decoder:** Takes the higher-level features and restores their spatial resolution for precise segmentation of tumour/nerve regions. This is done through up-sampling operations, such as the  $2 \times 2$  transposed convolutions used in the original paper. Towards the end, a network in a network ( $1 \times 1$  convolution) [38] is applied to produce  $C$  channels, where  $C$  is the number of output classes. In the case of tumour/nerve binary segmentation,  $C = 2$ . If multiple segmentation is used,  $C = 3$ . The spatial dimensions are also resized to match the original patch dimensions.
- **Copy and Crop:** These are skip connections connecting each stage in the encoder to the corresponding stage in the decoder. The feature maps from the encoder are cropped to match that of the decoder and concatenated with it. Since the encoder has more information about the position of objects in the original image, whereas the decoder contains the abstraction of features, combining them produces a rich, accurate segmentation map.

[21], [23], [24], [25] use U-Net in some part of their architecture. U-Net is also very flexible and can facilitate learning paradigms like transfer learning [39], which is very useful given that most medical imaging tasks have a limited training data pool that is better suited to fine-tuning than training from scratch. [21] and [23] replace the U-Net encoder with different architectures, such as Inception-Resnet-v2 [40] and EfficientNetB0 through B4 [41]. There are three main reasons for this:

1. **Pre-training:** The original authors pre-train their networks on large, open-source databases, giving the network a head-start. This improves segmentation performance upon fine-tuning with ground truth segmentation maps from a limited training data corpus, and it is highly relevant for PNI detection as seen in 3.
2. **Complexity:** The UNet encoder is relatively shallow in comparison with Inception-Net and EfficientNet. The substitution with deeper encoders allows for capturing more intricate patterns and learning more complex hierarchies. EfficientNet is also more computationally efficient.
3. **Residual Learning:** Skip connections are key to network robustness and training given their depth, allowing the neural network to learn the identity function and preventing exploding or vanishing gradients.

One other strategy involves ensemble models, as seen in [25]. Pixel-wise probabilities are averaged across a set of U-Net models (soft-voting), improving accuracy and stability, and reducing sensitivities to anomalies. These increase the model’s robustness against blurry sections of the WSI, for instance, while inferencing. [24] uses a fully unsupervised approach initially, implementing U-Net to approximate regions containing PNI in conjunctions with decision processes inspired by pathologist insight. This can be regarded as a pre-training step.

### 5.1.2 Other models

[22] uses Feature Pyramid Networks (FPNs) [42], which were originally designed for object detection. FPNs have a bottom-up pathway that produces feature maps at progressively lower resolutions (resembling a pyramid shape) using standard convolutions and pooling, followed by a top-down pathway where the feature maps are up-sampled and combined with the bottom-up pathway to learn features of the PNI junction at multiple scales. This allows the network to capture local information (precise junction boundary) while also considering broader context information. [26] uses U-Net++, which is a deeply supervised and more complex U-Net architecture [43]. It introduces nested skip connections with dense layers, allowing for features in skip pathways to be re-used as they are merged with the decoder's feature maps. The introduction of supervision in the hidden layers also improves gradient flow, stabilizing training and improving model convergence.

## 5.2 Object Detection Models

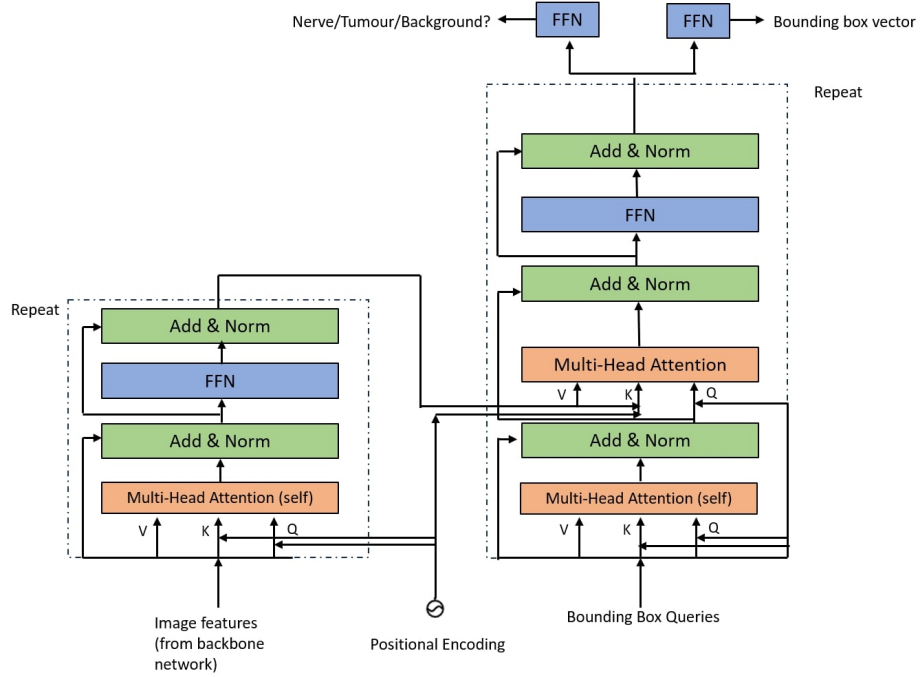


**Fig. 4:** Detection Transformer Model

To detect nerve bounding boxes, [26] utilizes the Detection Transformer (DETR) [44]. It employs a Transformer architecture where object detection is framed as a sequence prediction problem. Self-attention is applied to compute the relationships

between image features and object queries. An encoder takes in image features (usually an outcome of a backbone network, like ResNet101) and encodes them into keys (**K**) and values (**V**). A set number of queries (that can be likened to anchor boxes in traditional object detection models) are framed. The decoder inputs the queries and uses **K** and **V** to produce pairs of bounding box coordinates and class labels. A special class label,  $\phi$ , is used to denote a background bounding box. This is useful because the number of queries is much larger than the number of nerves in the patch, and excess queries are returned as background bounding boxes.

### 5.3 Classifiers

Upon obtaining segmented patches, they are post-processed (removing small, noisy predictions) and recombined into the WSI. After this, depending on the approach listed in 2, different methods are used to make either WSI-level or patient-level predictions.

- **Junction segmentation:** [22] makes a simple prediction by taking the largest probability per patch and applying average pooling across all patches to produce the WSI probability, which is then used for WSI-level classification. [23] is more sophisticated. It first finds matching pairs of predicted and ground truth lines by drawing bounding boxes at 150% scale around all instances within a WSI and looking for an intersection between the enlarged predicted and ground truth boxes. Then, the average minimum distances between lines in matching pairs and the intersection over the union (IoU) of their masks are used to calculate a single metric, *Dist\_Score*, whose value is compared with a fixed threshold to determine whether the prediction is a false positive, true positive, or false negative.
- **IoB and Area of Segmented Fields:** [21] counts  $Area_{nervemap} \cap Area_{tumormap} \neq 0$  as a PNI. [26] is more sophisticated and uses the intersection over bounding box (IoB) metric and predicts PNI positive only if  $IoB > 0.12$  rather than flagging any intersection as positive. 
$$IoB = \frac{A_{nerveBox} \cap A_{tumorMap}}{A_{nerveBox} \cup A_{tumorMap}}$$
- **End-to-End Neural network classification:** [25] uses Xception, a modified Inception Network with depth-wise separable convolutions within Inception blocks, simplifying model workflow [45]. Global max-pooling layers are added to the end of the standard Xception network, followed by fully connected layers leading up to a sigmoid activation function. Max pooling is used over patches to assign WSI (core) and subject probabilities for PNI. Global max-pooling and average-pooling for junction and end-to-end classification on an image  $x$  can largely be summarised as follows:

$$p_{x,avg} = AveragePool(x) = \frac{1}{|patches(x)|} \sum_{i \in patches(x)} p(y_i = 1)$$

$$p_{x,max} = MaxPool(x) = \underset{i \in patches(x)}{\operatorname{argmax}} p(y_i = 1)$$

Global max-pooling can identify highly discriminating, dominant regions in WSIs. Although it ignores broader contextual information, it is more appropriate for PNI detection as nerve-tumour interactions leading to highly activated patch probabilities can be captured without diluting it with irrelevant background information.

## 5.4 Loss Functions

Standard loss functions are used for all tasks:

$$\text{Binary Cross Entropy} = -\frac{1}{N} \sum_{i=1}^N [y_i \log(p_i) + (1 - y_i) \log(1 - p_i)]$$

$$\text{Dice Loss} = 1 - \frac{2 \cdot \text{TP}}{2 \cdot \text{TP} + \text{FP} + \text{FN}}$$

$$\text{Bipartite Loss} = \sum_{i=1}^N \max(0, \text{Margin} - \text{Sim}(\hat{y}_i, y_i))$$

Binary cross entropy measures the direct deviation between predicted probabilities and the ground truth PNI labels. Dice Loss penalizes overlap between the predicted and ground truth masks, with a lower Dice coefficient indicating more deviation. The version of the dice loss above is relevant only to binary segmentation problems. [26] uses Bipartite loss to tune DETR’s bounding boxes. A similarity function is used to measure the deviation between predicted and actual nerve-bounding boxes; a margin indicates the maximum similarity allowable on a single box to be able to contribute to the loss. All works except [25] and [26] utilize a loss combination technique to link the two different stages leading up to PNI classification together. [25] and [26] are orthogonalized and apply the loss functions independently.

## 6 Evaluation

### 6.1 Types of Evaluation Metrics

		Prediction outcome (p)		
		+	-	total
actual value (g)	+	True Positive (TP)	False Negative (FN)	P'
	-	False Positive (FP)	True Negative (TN)	N'
total		P	N	

#### 6.1.1 Classification Metrics

Classification can be performed at different levels: patch level, slide level, or patient level. Higher-level classification metrics, such as slide-level or patient-level, are more

desirable because they better reflect the performance of the algorithm in a clinical context. This is because these metrics directly align with the inputs used by pathologists, who typically work with whole slides or regions of interest (ROIs) rather than individual patches. Here are the classification metrics used for PNI recognition:

1. Precision/Positive predictive value (PPV):  $\frac{TP}{P}$ . A low PPV implies that the algorithm is aggressively categorizing cases as PNI and raising false alarms, which may waste pathologists' time if used as a flag for further review.
2. Sensitivity:  $\frac{TP}{P_r}$ . A low sensitivity indicates that the algorithm is missing actual cases of PNI; it may benefit from decreasing regularization in the network or gathering more training patches.
3. Specificity:  $\frac{TN}{N_r}$ . Similar to PPV, but focuses on negative predictions. A low specificity indicates that the algorithm is classifying a large number of actual negatives as positives (unable to identify non-PNI regions).
4. Negative Predictive Value (NPV):  $\frac{TN}{N}$ . Akin to sensitivity, but focuses on negative predictions. A low NPV indicates that the model is classifying a lot of positives as negatives and missing cases of PNI.
5. AUC-ROC: The algorithm's confidence threshold is adjusted. This could involve adjusting the probability threshold across pixels for a positive prediction or, in the case of bespoke rule-based classifiers, adjusting the critical value of IoB/distance which classifies a sample of PNI. The precision and sensitivity (recall) are plotted with varying thresholds. AUC is the area under this curve. A low AUC shows poor class distinguishing abilities.
6. F1:  $\frac{2 \times \text{Precision} \times \text{Sensitivity}}{\text{Precision} + \text{Sensitivity}}$ . The harmonic mean of Precision and Sensitivity. It provides a single-valued evaluation metric.

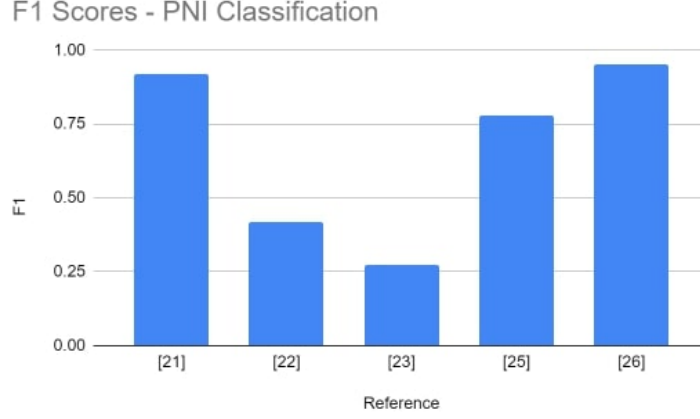
From Figure 5, we see that the highest F1 score is achieved by [26], which uses the rule-based IoB classifier at the end of a multi-stage segmentation and object detection approach. Closely following is [21], which categorizes any overlap in segmented nerve and tumour fields as PNI. [21] is more conservative, avoiding false positives and increasing precision in comparison to [26], even though it uses a less sophisticated classifier. This might be because segmentation masks are generally more precise [46] than bounding boxes, justifying the simpler approach to discriminating PNI from non-PNI that [21] uses in comparison to [26]. The Xception ensemble used in [25] directly calculates patch-wise probabilities and extrapolates them to the patient and core level. This is an overtly orthogonalized approach that sacrifices spatial context derived from tumour and nerve segmentation, resulting in poorer performance. Interestingly, while moving to a higher context (from core to subject) might tend to introduce more random noise in the predictions, the F1 score for patient classification is higher by 0.04. Lastly, [22] and [23] achieve very low F1 scores likely due to the limited data pool and the inclusion of several types of cancer with different boundary appearances.

### 6.1.2 Segmentation Metrics

Segmentation metrics are measured at a pixel level after thresholding prediction masks and recombining all patches into the WSI. Let  $P$  and  $G$  represent the prediction and ground truth WSI-level masks. IoU defines the common area between  $P$  and  $G$  as a

Classification (PNI Recognition) Performance of the models					
Reference	[21]	[22]	[23]	[25]	[26]
Model	Rule-Based (Area of segmented fields)	FPN (segment), Rule (Classify) (Max-Pooling on segmented junctions)	U-net (segment), Rule (classify) (Max-Pooling on segmented junctions)	Xception Ensemble of 10 (PNI field)	Rule-Based (IoB)
Precision	0.95	-	-	Cores: 0.67 Subjects: 0.69	0.933
Sensitivity	0.9	-	-	Cores: 0.87 Subjects: 0.94	0.972
Specificity	0.95	-	-	Cores: 0.97 Subjects: 0.91	-
NPV	0.9	-	-	Cores: 0.99 Patients: 0.99	-
AUC-ROC	$0.92 \pm 0.078$	-	-	Cores: $0.98 \pm 0.01$ Subjects: $0.96 \pm 0.03$	-
F1	0.92	0.416	0.2747	Cores: 0.76 Subjects: 0.80	0.952

(a) Table of Classification metrics



(b) F1 Scores

**Fig. 5:** Classification metrics: Data

ratio of their total areas.

$$\text{IoU} = \frac{P \cap G}{P \cup G}$$

We define the pixel-wise segmentation error as follows:

$$E(g, p, c) = \begin{cases} TP & \text{if } g = c, p = c \\ TN & \text{if } g \neq c, p \neq c \\ FP & \text{if } g \neq c, p = c \\ FN & \text{if } g = c, p \neq c \end{cases}$$

For a particular class  $c$ , we can define the number of true positives as:

$$TP_c = \sum_{g \in G, p \in P} |(g, p)| : E(g, p, c) = TP$$

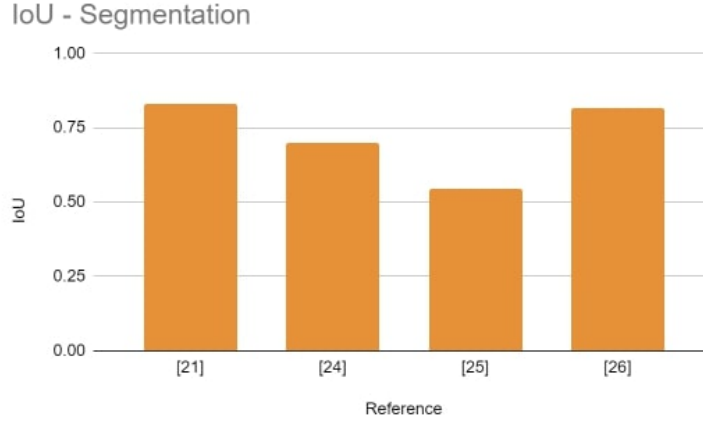
Thus, we can also define  $TN_c$ ,  $FP_c$ ,  $FN_c$ . Using these we can define  $\text{Precision}_{\text{seg}}$ ,  $\text{Sensitivity}_{\text{seg}}$  by summing over all classes  $C$ . For binary segmentation,  $C = 0$  (Background) and 1 (Nerve/Tumor/Junction). For multi-class segmentation,  $C = 0$  (Background) and 1 (Tumor) and 2 (Nerve).<sup>‡</sup>

$$\text{Precision}_{\text{seg}} = \sum_{c \in C} \frac{TP_c}{TP_c + FP_c} \quad \text{Sensitivity}_{\text{seg}} = \sum_{c \in C} \frac{TP_c}{TP_c + FN_c}$$

From Figure 6(a), it is generally observed that tumour segmentation is a harder task

Segmentation Performance of the models				
Reference	[21]	[24]	[25]	[26]
Model	Binary segmentation: UNet (Nerve) DeepLabv3+ (Tumor)	HCA + Binary Segmentation UNet (Nerve, Tumor)	Binary segmentation: UNet Ensemble of 10 (PNI field)	Binary segmentation: UNet++ (Tumor)
Sensitivity	Nerve: 0.943 Tumor: 0.903	Nerve: 0.85 Tumor: 0.57	-	0.81
Precision	Nerve: 0.937 Tumor: 0.839	-	-	0.87
F1	Nerve: 0.940 Tumor: 0.869	-	-	0.841
IoU	Nerve: 0.887 Tumor: 0.769	Nerve: 0.79 Tumor: 0.61	0.50 ± 0.045	0.815

(a) Table of Segmentation Metrics



(b) IoU Scores

**Fig. 6:** Segmentation metrics: Data

than nerve segmentation, with lower IoU scores on the test set. This is because while nerves vary in shape and size across multiple organs, cancerous regions can be highly irregular and diffuse across multiple patches of the same type of cancer [47]. Complex pipelines with more novel segmentation models (eg: UNet++ and EfficientNet-B3 in [26] compared to the simpler UNet in [25]) demonstrate better performance. It would

<sup>‡</sup>Please note that [24] also examines False alarm rate for segmentation. However, it has not been included in this paper as there is no comparison with other literature.

have been interesting to examine the segmentation performance on PNI junctions, observing the effect of their fine-grained nature compared to larger PNI, nerve, or tumour fields. Unfortunately, [22] and [23] do not list it as the rules of the PAIP 2021 challenge ranked teams based on the F1 score.

### 6.1.3 Bespoke Metrics - Bounding box detection

As [26] uses a DETR for predicting bounding boxes around nerves, it uses the **mean average precision (mAP)**[46] metric to evaluate the accuracy of the bounding boxes. Let  $\kappa$  represent the IoU threshold and  $C$  represent the class.

$$mAP_{\kappa} = \frac{1}{C} \sum_{c \in C} AP_{\kappa, c}$$

As discussed in 5, the decoder of the detection transformer outputs  $Q$  bounding boxes and softmax vectors containing the confidence scores (probabilities) for each class i.e. nerve and background. For each class, all bounding boxes at the slide level are compared against their ground truth bounding boxes, and an IoU is calculated. If  $IoU > \kappa$ , then the predicted bounding box is counted as a true positive ( $TP$ ). Otherwise, it is counted as a false positive ( $FP$ ) because of insufficient overlap. A ground truth without any matching predictions will be counted as a false negative ( $FN$ ). Based on  $TP, FP, FN$ , precision and recall scores can be calculated grouped by the confidence scores for that class. The minimum value for the confidence score is varied, leading to a receiver-operating curve with various values of precision and recall whose area will yield  $AP_{\kappa, c}$ . This process is repeated for both classes and their mean,  $mAP_{\kappa}$  is calculated. The authors in [26] use two values of  $\kappa$ , yielding  $mAP_{0.75} = 0.587$  and  $mAP_{0.50} = 0.775$  as the best performance. This metric cannot be compared with other works as it considers both the accuracy of bounding box classification (nerve, tumour) and localization, while all other metrics only denote performance in a single aspect.

## 6.2 Ablation Studies

<sup>‡</sup> An ablation study refers to further study undertaken by tweaking the components of the DL model and observing the effect it has on its performance. They are important in determining critical elements of the model, which must be sustained through any further iterations, and any points of improvement.

### 6.2.1 Effect of Transfer Learning

Transfer learning [39] is a learning paradigm wherein a neural network is pre-trained on a large dataset (for example, ImageNet [27]), where it learns to detect low-level features that can be useful in the segmentation of medical structures, including nerve and tumour. All authors have utilized pre-trained architectures and fine-tuned them using ground-truth annotations as seen in 5. [21] examined the effect of pre-training

---

<sup>‡</sup>Please note that [22] also studies the effect of implementing TTA and extracting overlapping patches from test images. These are not discussed as they are used to improve rankings on the PAIP 2021 challenge and are computationally infeasible for integration into the inference pipeline.



on the performance of Segformer’s multi-class segmentation performance, showing a 29% and a 25% increase in IoU for Tumor and Nerve segmentation respectively; furthermore, the F1 scores also increased by 17.3% for tumour and 16.4% for nerve segmentation respectively. These metrics reinforce the importance of pre-training on a task with limited data availability.

### 6.2.2 Boundary Dilation and Loss combination

[23] examines the performance improvement brought about by changing the extent of boundary dilation (see section 4) and using both the standalone dice-loss and combining it with binary cross entropy. Changing the radius of the morphological dilation operator from  $r = 1$  to  $r = 2$  improves the detection F1-score by an average of only 2.6%, suggesting that the model captures the most relevant junction information with the smaller radius. However, the inclusion of binary cross entropy improves the F1 score substantially, by an average of 41.5%. Integrating the end goal (PNI detection) into the segmentation task’s training allows the model to achieve a balance between pixel-level accuracy and region-level outcome.

### 6.2.3 Computational Complexity

[26] examines the performance of various segmentation and object detection models, documenting their (Floating point operations per second) FLOPs and the number of parameters, opening up the scope for implementing an accuracy-complexity trade-off scheme for integration into pathology labs where algorithms can flag images for review. For example, they show that using a UNet++ segmenter, a detection transformer model, and a shared EfficientNet backbone is 74% more efficient; the decrease in recognition F1 is only 15%. Similarly, traditional object detection algorithms, such as YOLO and Faster-R-CNN detect nerves at  $\sim 40 - 50\%$  of the resource load as DETR with only a 5 - 15% reduction in *mAP*.

## 6.3 Algorithm Error Analysis

Due to the high stakes involved in medical imaging (and PNI detection especially so), carrying out error analysis is crucial [20]. The following systematic inaccuracies were observed across [21], [25], [26].

- **Misclassified Tumor:** Benign glands in the vicinity, Entrapped neural bundles resembling stroma, Inflammatory cells.
- **Misclassified Nerve:** Smooth muscle cells (resemble Schwann cells in their spindle shape), Mucinous Fibroplasia (in prostate adenocarcinoma only)

Histological tissue with similar structural features to nerves and tumours is bound to be misidentified when working with a small field like WSI patches. These can be dealt with using domain-specific filtering rules or ensemble models to refine the model’s masks. However, consideration of increasing inference times is necessary here as well, keeping in mind the ease of distinguishing the above features from nerve/tumour manually if the algorithm is merely flagging images for further review.

## 7 Discussion

This section discusses the issues associated with current models and the scope for future research with a focus on the ability to deploy these models to diagnose PNI from real-time patient data.

### 7.1 Combining Image analysis with blood markers

Inflammatory response in cancer is associated with several blood markers, for example, Prostate-specific antigen (PSA) has been shown to play a crucial role in the prognosis of prostate cancer and is associated with inflammation [48]. Likewise, it has been shown that Carcinoembryonic Antigens are a sign of inflammation, including PNI [49]. Using a multi-stage model to combine existing WSI analysis techniques with a separate machine-learning algorithm could add value to PNI detection. For example, anomaly detection algorithms could flag patients with abnormal biomarker levels, refining predictions when combined with image-based features. Techniques like feature fusion could be applied to combine image features and biomarker data, leading to a more holistic prediction of PNI presence.

### 7.2 Integration into pathological workflows

Despite utilizing state-of-the-art models and achieving high benchmarks, most of the models discussed will fail to operate when deployed in a pathology lab because of the large computational complexities involved in training and making predictions on them; this will be especially problematic when using real-time pathologist annotations on wrong predictions to improve the model. Based on the ablative experiments in 6.2.3, it might be more practical to implement a trade-off strategy between computational complexity and model accuracy. To do this, a systematic sensitivity analysis on a metric representing the objective accuracy (accuracy bearing in mind complexity) of the model will be required, with the level of trade-off stemming from external factors specific to the lab eg. the number of samples digitized into WSIs every day, the number of reports submitted by pathologists daily, etc. For example:

$$C = f(L_{Conv}, U_{Conv}, L_{pool}, U_{pool}, \dots, model\_size, memory\_usage)$$

$$M = \frac{A}{1 + \lambda C}$$

$C$ , the complexity, can be computed as a learned function  $f(\cdot)$  of the number of layers of a specific type  $k$ ,  $L_k$ , the number of units in the layer  $U_k$ , model storage and memory use, etc. The trade-off metric,  $M$  is designed so that  $M \propto A$ , the model's accuracy (eg: IoU/F1) and  $M \propto \frac{1}{C}$ . The hyperparameter  $\lambda$  indicates the relative importance of complexity with respect to accuracy, and can be tuned to the aforementioned external factors.  $\frac{\delta M}{\delta A} = \frac{1}{1 + \lambda C}$  and  $\frac{\delta M}{\delta T} = -\frac{\lambda A}{(1 + \lambda T)^2}$  can be calculated to evaluate the sensitivity of  $M$  when components of  $C$  and the accuracy  $A$  are varied, offering insight to converge at a workable operating point [50]. Moreover, strategies like model pruning [51] and quantization [52] could be considered to reduce the model's size and computational burden while still maintaining accuracy. Since

most hospitals run AI algorithms on cloud GPUs, another avenue is examining how the models perform on cloud TPUs and GPUs to produce usage budget estimates for cost-benefit analysis by hospitals. Ultimately, cost-benefit analysis serves as a vital tool for decision-makers in healthcare, ensuring that the deployment of advanced diagnostic technologies is economically viable and beneficial for patient care.

### 7.3 Explainability and inter-observer agreement

A critical element of deployment in a pathology lab is pathologist-friendliness. The predictions of the model should be explainable through visual heat maps displaying areas that activated the model’s output, in case of a PNI positive outcome. These insights are valuable even when pathologists can see the segmentation maps as specific edges, textures and colours that the model diagnoses as nerve, tumour, or a PNI junction can be visualized. Saliency maps [53] are a good tool to use here.

$$S(x) = \left| \frac{\delta M(x)}{\delta x} \right| \quad S_{norm}(x) = \frac{S(x) - \min(S(x))}{\max(S(x)) - \min(S(x))}$$

$S(x)$  represents the saliency map of the patch  $x$ . This is the gradient of the output of the segmentation or classification model  $M(x)$  with respect to the input image. The partial derivative helps us identify regions that are most sensitive to changes in input pixel values (and thus, have a high gradient). They are typically normalized into  $S_{norm}(x)$ . Grad-CAM [54] implements a similar technique albeit by calculating gradients with respect to the last convolutional layer to produce intermediate weights, then multiplying them with the output of the last convolutional layer to produce the heat map. Grad-CAM provides better insight into how models use spatial arrangements from a higher level of abstraction (the last layer) and can offer highly relevant insight for PNI detection. Tuning inter-observer agreement is a strategy to improve concordance with pathologists and mimic their thought process. Cohen’s Kappa is a measure of inter-observer agreement [55]:

$$\kappa = \frac{p_o - p_e}{1 - p_e}$$

$p_o$  measures the observed agreement between the two raters, while  $p_e$  is the expected agreement by chance, based on the marginal proportion of each of the rater’s decisions.  $\kappa$  is a robust statistical measure that can be explicitly referenced in the loss function, motivating the model to maximize it. The two raters would be the ground truth pathologist and the DL algorithm. The ground truth pathologist used in the calculation can also be representative of the average predictions of multiple expert pathologists, which would further work in favour of the optimizing objective. In fact, [25] performs a further experiment, having 4 pathologists (including the model) annotate the test set and documenting the mean pairwise  $\kappa$  value between each pathologist and the other three. For the human pathologists, this resulted in  $0.684 \leq \kappa \leq 0.754$ , and for the model,  $\kappa$  was 0.740, a value within the aforementioned range, demonstrating the calibre of these models and the extent of agreement that can be achieved when explicitly tuned to maximize  $\kappa$ .

## 7.4 Noise in input data from preserved pathological samples

Most pathology labs use sequential sample processing. In high-volume labs, improper preservation and digitization after a non-trivial storage period may change the distribution of data, making it different from the training distribution. Sometimes, samples need to be re-digitized after a few months as well, which poses the same problem. The algorithm must be made noise-resistant. While data augmentation assists to an extent by introducing random noise through colour and contrast adjustment, more systematic solutions governing data collection and pre-processing must be considered. It would be beneficial to collect temporal data and curate a dataset containing PNI WSIs in different stages of degradation, which the model can familiarize itself with. Neural networks have also been applied to image restoration [56]. A small auxiliary model can be trained to restore images older than a pre-decided span. Denoising algorithms, such as Gaussian filters are also feasible due to their efficient 1D convolution implementation [56].

## 7.5 Different staining techniques

While this section does not contain implementation avenues, it is still an interesting prospect. The datasets used in most medical imaging papers, including this one, are stained with Hematoxylin and Eosin (H&E). It is commonplace and will distinguish between most structures clearly, but for PNI, it may not always provide sufficient contrast to differentiate neural structures from adjacent tissues. Other stains, such as S100 (identification of Schwann cells), Neurofilament stain (general detection of nerve tissue), etc. can enhance the expression of PNI. This strategy is not practical to implement as the other stains are more expensive and not suited to general cancer recognition, but further study on this concept opens up avenues for exploring how specialized imaging techniques could complement AI-driven analysis, pushing the boundaries of precision.

## 8 Conclusion

This survey highlights the immense potential of DL in revolutionizing PNI detection, a critical component in cancer prognosis. By offering a structured analysis of existing models, datasets, and evaluation metrics, this paper lays the foundation for future research aimed at translating these models into clinical practice. Moving forward, efforts should focus on developing more comprehensive datasets encompassing a larger number of cancer types and sample preservation parameters, improving model interpretability and concordance with pathologists, and ensuring that these AI tools can be integrated into real-world workflows with cost-benefit analyses for hospitals and scalable models. The next step is for researchers and clinicians to collaborate closely, ensuring that AI-driven diagnostic tools are both effective and ethically implemented for the benefit of patient care.

## Acronyms

**AI** Artificial Intelligence  
**DETR** Detection Transformer  
**DL** Deep Learning  
**FLOPs** Floating Point Operations per Second  
**FPN** Feature Pyramid Networks  
**GAN** Generative Adversarial Networks  
**H and E** Hematoxylin and Eosin Stain  
**IoB** Intersection over Bounding Box  
**IoU** Intersection over Union  
**mAP** Mean Average Precision  
**PNI** Perineural Invasion  
**PPV** Positive Predictive Value  
**PSA** Prostate-Specific Antigen  
**WSI** Whole Slide Image

## Conflict of Interest

The authors declare no competing financial or non-financial interests that could have influenced the work reported in this paper. This review was conducted independently, without any external influence from entities that could benefit from the findings or outcomes.

## Data Availability

This article is a systematic review, and no primary datasets were generated or analyzed during this study. All data used for this review is publicly available through the articles cited in the references section. The studies referenced can be accessed via their respective publishers' platforms or repositories. Detailed information regarding each dataset, methodologies, and findings can be found in the cited literature.

## References

- [1] Batsakis, J.G.: Nerves and neurotropic carcinomas. *Ann Otol Rhinol Laryngol* **94**(4 Pt 1), 426–427 (1985)
- [2] King, R.: 6. Peripheral Nerve Disorders, pp. 32–37. John Wiley & Sons, Ltd, Chichester, UK (2014). <https://doi.org/10.1002/9781118618424.ch6>
- [3] Amit, M., Binenbaum, Y., Trejo-Leider, L., Sharma, K., Ramer, N., Ramer, I., Agbetoba, A., Miles, B., Yang, X., Lei, D., Bjørndal, K., Godballe, C., Mücke, T., Wolff, K.-D., Eckardt, A.M., Copelli, C., Sesenna, E., Palmer, F., Ganly, I., Patel, S., Gil, Z.: International collaborative validation of intraneural invasion as a prognostic marker in adenoid cystic carcinoma of the head and

neck. *Head & Neck* **37**(7), 1038–1045 (2015) <https://doi.org/10.1002/hed.23710>  
<https://onlinelibrary.wiley.com/doi/pdf/10.1002/hed.23710>

- [4] Larson, D.L., Rodin, A.E., Roberts, D.K., O'Steen, W.K., Rapperport, A.S., Lewis, S.R.: Perineural lymphatics: Myth or fact. *The American Journal of Surgery* **112**(4), 488–492 (1966) [https://doi.org/10.1016/0002-9610\(66\)90309-6](https://doi.org/10.1016/0002-9610(66)90309-6). Papers of the Society of Head and Neck Surgeons
- [5] Akert, K., Sandri, C., Weibel, E.R., Peper, K., Moor, H.: The fine structure of the perineural endothelium. *Cell and Tissue Research* **165**(3), 281–295 (1976) <https://doi.org/10.1007/BF00222433>
- [6] Chen, S.-H., Zhang, B.-Y., Zhou, B., Zhu, C.-Z., Sun, L.-Q., Feng, Y.-J.: Perineural invasion of cancer: a complex crosstalk between cells and molecules in the perineural niche. *Am. J. Cancer Res.* **9**(1), 1–21 (2019)
- [7] Zhang, L.J., Wu, B., Zha, Z.L., Qu, W., Zhao, H., Yuan, J., Feng, Y.J.: Perineural invasion as an independent predictor of biochemical recurrence in prostate cancer following radical prostatectomy or radiotherapy: a systematic review and meta-analysis. *BMC Urol* **18**(1), 5 (2018)
- [8] Kim, H.E., Park, S.Y., Kim, H., Kim, D.J., Kim, S.I.: Prognostic effect of perineural invasion in surgically treated esophageal squamous cell carcinoma. *Thorac Cancer* **12**(10), 1605–1612 (2021) <https://doi.org/10.1111/1759-7714.13960>
- [9] Duraker, N., man, S., Can, G.: The significance of perineural invasion as a prognostic factor in patients with gastric carcinoma. *Surg Today* **33**(2), 95–100 (2003) <https://doi.org/10.3390/jpm12060962>
- [10] Tanaka, A., Watanabe, T., Okuno, K., Yasutomi, M.: Perineural invasion as a predictor of recurrence of gastric cancer. *Cancer* **73**(3), 550–555 (1994) [https://doi.org/10.1002/1097-0142\(19940201\)73:3<550::aid-cnrc2820730309>3.0.co;2-0](https://doi.org/10.1002/1097-0142(19940201)73:3<550::aid-cnrc2820730309>3.0.co;2-0)
- [11] Stojkovic Lalosevic, M., Milovanovic, T., Micev, M., Stojkovic, M., Dragasevic, S., Stulic, M., Rankovic, I., Dugalic, V., Krivokapic, Z., Pavlovic Markovic, A.: Perineural invasion as a prognostic factor in patients with stage I-III rectal cancer - 5-year follow up. *World J Gastrointest Oncol* **12**(5), 592–600 (2020) <https://doi.org/10.4251/wjgo.v12.i5.592>
- [12] Chi, A.C., Katabi, N., Chen, H.S., Cheng, Y.L.: Interobserver Variation Among Pathologists in Evaluating Perineural Invasion for Oral Squamous Cell Carcinoma. *Head Neck Pathol* **10**(4), 451–464 (2016) <https://doi.org/10.1007/s12105-016-0722-9>
- [13] Holthoff, E.R., Jeffus, S.K., Gehlot, A., Stone, R., Erickson, S.W., Kelly, T., Quick, C.M., Post, S.R.: Perineural Invasion Is an Independent Pathologic Indicator of Recurrence in Vulvar Squamous Cell Carcinoma. *Am J Surg Pathol* **39**(8),

- 1070–1074 (2015) <https://doi.org/10.1097/PAS.0000000000000422>
- [14] Peng, J., Sheng, W., Huang, D., Venook, A.P., Xu, Y., Guan, Z., Cai, S.: Perineural invasion in pT3N0 rectal cancer: the incidence and its prognostic effect. *Cancer* **117**(7), 1415–1421 (2011) <https://doi.org/10.1002/cncr.25620>
  - [15] Yan, F., Cheng, Y.L., Katabi, N., Nguyen, S.A., Chen, H.S., Morgan, P., Zhang, K., Chi, A.C.: Interobserver Variation in Evaluating Perineural Invasion for Oral Squamous Cell Carcinoma: Phase 2 Survey Study. *Head Neck Pathol* **15**(3), 935–944 (2021) <https://doi.org/10.1007/s12105-021-01321-9>
  - [16] Schneider, J., Vlachos, M.: A Survey of Deep Learning: From Activations to Transformers (2024). <https://doi.org/10.48550/arXiv.2302.00722>
  - [17] Nirschl, J.J., Janowczyk, A., Peyster, E.G., Frank, R., Margulies, K.B., Feldman, M.D., Madabhushi, A.: A deep-learning classifier identifies patients with clinical heart failure using whole-slide images of H&E tissue. *PLoS One* **13**(4), 0192726 (2018) <https://doi.org/10.1371/journal.pone.0192726>
  - [18] Jha, A., Yang, H., Deng, R., Kapp, M.E., Fogo, A.B., Huo, Y.: Instance segmentation for whole slide imaging: end-to-end or detect-then-segment. *Journal of Medical Imaging* **8**(1), 014001 (2021) <https://doi.org/10.1117/1.JMI.8.1.014001>
  - [19] Feng, R., Liu, X., Chen, J., Chen, D.Z., Gao, H., Wu, J.: A deep learning approach for colonoscopy pathology wsi analysis: Accurate segmentation and classification. *IEEE Journal of Biomedical and Health Informatics* **25**(10), 3700–3708 (2021) <https://doi.org/10.1109/JBHI.2020.3040269>
  - [20] Litjens, G., Kooi, T., Bejnordi, B.E., Setio, A.A.A., Ciompi, F., Ghafoorian, M., Laak, J.A.W.M., Ginneken, B., Sánchez, C.I.: A survey on deep learning in medical image analysis. *Medical Image Analysis* **42**, 60–88 (2017) <https://doi.org/10.1016/j.media.2017.07.005>
  - [21] Jung, J., Kim, E., Lee, H., Lee, S.H., Ahn, S.: Automated hybrid model for detecting perineural invasion in the histology of colorectal cancer. *Applied Sciences* **12**(18) (2022) <https://doi.org/10.3390/app12189159>
  - [22] Nateghi, R., Pourakpour, F.: Perineural Invasion Detection in Multiple Organ Cancer Based on Deep Convolutional Neural Network (2021). <https://doi.org/10.48550/arXiv.2110.12283>
  - [23] Park, Y., Park, J., Jang, G.-J.: Efficient perineural invasion detection of histopathological images using u-net. *Electronics* **11**(10) (2022) <https://doi.org/10.3390/electronics11101649>
  - [24] Borsekofsky, S., Tsuril, S., Hagege, R.R., Hershkovitz, D.: Perineural invasion

- p>detection in pancreatic ductal adenocarcinoma using artificial intelligence. Scientific Reports
- 13**
- (1), 13628 (2023)
- <https://doi.org/10.1038/s41598-023-40833-y>
- [25] Kartasalo, K., m, P., Ruusu vuori, P., Samaratunga, H., Delahunt, B., Tsuzuki, T., Eklund, M., Ege vad, L.: Detection of perineural invasion in prostate needle biopsies with deep neural networks. Virchows Arch **481**(1), 73–82 (2022) <https://doi.org/10.1007/s00428-022-03326-3>
  - [26] Hu, Z., Deng, Y., Lan, J., Wang, T., Han, Z., Huang, Y., Zhang, H., Wang, J., Cheng, M., Jiang, H., Lee, R.-G., Du, M., Tong, T., Gao, Q., Chen, G.: A multi-task deep learning framework for perineural invasion recognition in gastric cancer whole slide images. Biomedical Signal Processing and Control **79**, 104261 (2023) <https://doi.org/10.1016/j.bspc.2022.104261>
  - [27] Deng, J., Dong, W., Socher, R., Li, L.-J., Li, K., Fei-Fei, L.: Imagenet: A large-scale hierarchical image database. In: 2009 IEEE Conference on Computer Vision and Pattern Recognition, pp. 248–255 (2009). <https://doi.org/10.1109/CVPR.2009.5206848>
  - [28] Janowczyk, A., Madabhushi, A.: Deep learning for digital pathology image analysis: A comprehensive tutorial with selected use cases. J Pathol Inform **7**, 29 (2016) <https://doi.org/10.4103/2153-3539.186902>
  - [29] Challenge, G.: PAIP 2021 Challenge: Perineural Invasion in Multiple Organ Cancer (Colon, Prostate and Pancreatobiliary tract). Accessed: 2024-09-15 (2021). <https://paip2021.grand-challenge.org/>
  - [30] Eklund, M., m, T., Aly, M., Adolfsson, J., Wiklund, P., Brandberg, Y., Thompson, J., Wiklund, F., Lindberg, J., Presti, J.C., StLezin, M., Clements, M., Ege vad, L., nberg, H.: The Stockholm-3 (STHLM3) Model can Improve Prostate Cancer Diagnostics in Men Aged 50-69 yr Compared with Current Prostate Cancer Testing. Eur Urol Focus **4**(5), 707–710 (2018) <https://doi.org/10.1016/j.euf.2016.10.009>
  - [31] Kondylakis, H., Kalokyri, V., Sfakianakis, S., Marias, K., Tsiknakis, M., Jimenez-Pastor, A., Camacho-Ramos, E., Blanquer, I., Segrelles, J.D., López-Huguet, S., Barelle, C., Kogut-Czarkowska, M., Tsakou, G., Siopis, N., Sakellariou, Z., Bizopoulos, P., Drossou, V., Lalas, A., Votis, K., Mallol, P., Marti-Bonmati, L., Alberich, L.C., Seymour, K., Boucher, S., Ciarrocchi, E., Fromont, L., Rambla, J., Harms, A., Gutierrez, A., Starmans, M.P.A., Prior, F., Gelpi, J.L., Lekadir, K.: Data infrastructures for ai in medical imaging: a report on the experiences of five eu projects. European Radiology Experimental **7**(1), 20 (2023) <https://doi.org/10.1186/s41747-023-00336-x>
  - [32] Janowczyk, A., Madabhushi, A.: Deep learning for digital pathology image analysis: A comprehensive tutorial with selected use cases. Journal of Pathology Informatics **7**(1), 29 (2016) <https://doi.org/10.4103/2153-3539.186902>



- [33] Cossio, M.: Augmenting Medical Imaging: A Comprehensive Catalogue of 65 Techniques for Enhanced Data Analysis (2023). <https://doi.org/10.48550/arXiv.2303.01178>
- [34] Goodfellow, I.J., Pouget-Abadie, J., Mirza, M., Xu, B., Warde-Farley, D., Ozair, S., Courville, A., Bengio, Y.: Generative Adversarial Networks (2014). <https://doi.org/10.48550/arXiv.1406.2661>
- [35] TensorFlow: Data Augmentation. Accessed: 2024-09-15 (2024). [https://www.tensorflow.org/tutorials/images/data\\_augmentation](https://www.tensorflow.org/tutorials/images/data_augmentation)
- [36] PyTorch: Transforms. Accessed: 2024-09-15 (2024). <https://pytorch.org/vision/0.9/transforms.html>
- [37] Ronneberger, O., Fischer, P., Brox, T.: U-Net: Convolutional Networks for Biomedical Image Segmentation (2015). <https://doi.org/10.48550/arXiv.1505.04597>
- [38] Lin, M., Chen, Q., Yan, S.: Network In Network (2014). <https://doi.org/10.48550/arXiv.1312.4400>
- [39] Yosinski, J., Clune, J., Bengio, Y., Lipson, H.: How transferable are features in deep neural networks? (2014). <https://doi.org/10.48550/arXiv.1411.1792>
- [40] Szegedy, C., Liu, W., Jia, Y., Sermanet, P., Reed, S., Anguelov, D., Erhan, D., Vanhoucke, V., Rabinovich, A.: Going Deeper with Convolutions (2014). <https://doi.org/10.48550/arXiv.1409.4842>
- [41] Tan, M., Le, Q.V.: EfficientNet: Rethinking Model Scaling for Convolutional Neural Networks (2020). <https://doi.org/10.48550/arXiv.1905.11946>
- [42] Lin, T.-Y., Dollár, P., Girshick, R., He, K., Hariharan, B., Belongie, S.: Feature Pyramid Networks for Object Detection (2017). <https://doi.org/10.48550/arXiv.1612.03144>
- [43] Zhou, Z., Siddiquee, M.M.R., Tajbakhsh, N., Liang, J.: UNet++: A Nested U-Net Architecture for Medical Image Segmentation (2018). <https://doi.org/10.48550/arXiv.1807.10165>
- [44] Carion, N., Massa, F., Synnaeve, G., Usunier, N., Kirillov, A., Zagoruyko, S.: End-to-End Object Detection with Transformers (2020). <https://doi.org/10.48550/arXiv.2005.12872>
- [45] Chollet, F.: Xception: Deep Learning with Depthwise Separable Convolutions (2017). <https://doi.org/10.48550/arXiv.1610.02357>
- [46] Lin, T.-Y., Maire, M., Belongie, S., Hays, J., Perona, P., Ramanan, D., Dollár, P., Zitnick, C.L.: Microsoft coco: Common objects in context. In: Fleet, D., Pajdla,

- T., Schiele, B., Tuytelaars, T. (eds.) Computer Vision – ECCV 2014, pp. 740–755. Springer, Cham (2014). <https://doi.org/10.48550/arXiv.1405.0312>
- [47] Han, Z., Wei, B., Zheng, Y., Yin, Y., Li, K., Li, S.: Breast cancer multi-classification from histopathological images with structured deep learning model. *Scientific Reports* **7**(1), 4172 (2017) <https://doi.org/10.1038/s41598-017-04075-z>
  - [48] Elgamal, A.A., Petrovich, Z., Van Poppel, H., Baert, L.: In: Petrovich, Z., Baert, L., Brady, L.W. (eds.) *The Role of Prostate-Specific Antigen in the Management of Prostate Cancer*, pp. 179–197. Springer, Berlin, Heidelberg (1996). [https://doi.org/10.1007/978-3-642-60956-5\\_14](https://doi.org/10.1007/978-3-642-60956-5_14)
  - [49] Lee, T.-H., Kim, J.-S., Baek, S.-J., Kwak, J.-M., Kim, J.: Diagnostic accuracy of carcinoembryonic antigen (cea) in detecting colorectal cancer recurrence depending on its preoperative level. *Journal of Gastrointestinal Surgery* **27**(8), 1694–1701 (2023) <https://doi.org/10.1007/s11605-023-05761-2>
  - [50] Fernández-Moreno, M., Lei, B., Holm, E.A., Mesejo, P., Moreno, R.: Exploring the trade-off between performance and annotation complexity in semantic segmentation. *Engineering Applications of Artificial Intelligence* **123**, 106299 (2023) <https://doi.org/10.1016/j.engappai.2023.106299>
  - [51] Han, S., Pool, J., Tran, J., Dally, W.J.: Learning both Weights and Connections for Efficient Neural Networks (2015). <https://doi.org/10.48550/arXiv.1506.02626>
  - [52] Krishnamoorthi, R.: Quantizing deep convolutional networks for efficient inference: A whitepaper (2018). [10.48550/arXiv.1806.08342](https://arxiv.org/abs/1806.08342)
  - [53] Zeiler, M.D., Fergus, R.: Visualizing and Understanding Convolutional Networks (2013). <https://doi.org/10.48550/arXiv.1311.2901>
  - [54] Selvaraju, R.R., Cogswell, M., Das, A., Vedantam, R., Parikh, D., Batra, D.: Grad-cam: Visual explanations from deep networks via gradient-based localization. *International Journal of Computer Vision* **128**(2), 336–359 (2019) <https://doi.org/10.1007/s11263-019-01228-7>
  - [55] Cohen, J.: A coefficient of agreement for nominal scales. *Educational and Psychological Measurement* **20**(1), 37–46 (1960) <https://doi.org/10.1177/001316446002000104>
  - [56] Thakkar, J.D., Bhatt, J.S., Patra, S.K.: Self-supervised learning for medical image restoration: Investigation and finding. In: Singh, P., Singh, D., Tiwari, V., Misra, S. (eds.) *Machine Learning and Computational Intelligence Techniques for Data Engineering*, pp. 541–552. Springer, Singapore (2023). [https://doi.org/10.1007/978-981-99-0047-3\\_46](https://doi.org/10.1007/978-981-99-0047-3_46)